Geophysical Journal International

Geophys. J. Int. (2026) **244,** 1–15
Advance Access publication 2025 November 24
Research Paper

https://doi.org/10.1093/gji/ggaf470

A rock physics model for predicting the velocities of isotropic sediments hosting heterogeneously distributed gas hydrates

Xiangyu Zhu,[1,2] Weixin Pang,[1,2] Anyu Li,[3] Zhenyu Zhu,[1] Tao Liu,[4] Qi Fan,[1,2] Yang Ge,[1,2] Sourav K. Sahoo,[5] Angus I. Best[5] and Xuewei Liu[6]

[1] *CNOOC Research Institute Co., Ltd, Beijing* 100028*, China. E-mail:* *zhu96xiangyu@163.com*
[2] *State Key Laboratory of Offshore Natural Gas Hydrates,* Beijing 102209*, China*
[3] *School of Petroleum and Natural Gas Engineering, Chongqing University of Science and Technology, Chongqing 401331, China*
[4] *School of Ocean and Earth Science, Tongji University, Shanghai 200092, China*
[5] *National Oceanography Centre, Southampton SO*143*ZH, UK*
[6] *School of Geophysics and Information Technology, China University of Geosciences, Beijing* 100083*, China*

Accepted 2025 November 18. Received 2025 September 23; in original form 2025 March 18

SUMMARY

Elastic rock physics models are widely used to estimate the saturation of hydrate in isotropic sediments. However, for isotropic media, the influence of heterogeneously distributed hydrate on the *P*- and *S*-wave velocities remains unclear, leading to uncertainties in hydrate saturation estimates. To address this issue, in this work we proposed a double-solid-matrix model for predicting the velocities of sediments hosting heterogeneously distributed hydrates. A comparison of simulated velocities of our model and two rock physics schemes designed for homogeneous distributed hydrate (i.e. matrix-supporting and pore-floating models) show that, our model predicts higher *S*-wave velocity than matrix-supporting and pore-floating models, but yields similar *P*-wave velocity estimates as matrix-supporting model. We apply our model to two marine hydrate sites in the Cascadia margin: Site 1245 from Ocean Drilling Program Leg 204 and Site U1328 from International Ocean Drilling Program Expedition 311. Two locations yield similar results: velocity estimates from our model are much closer to downhole measurements than matrix-supporting and pore-floating models. Moreover, we estimate *in situ* hydrate saturation and clay concentration using our model, matrix-supporting model, and pore-floating model independently, and find that (i) hydrate saturations predicted by our model conform better with the saturations from chloride concentration and (ii) clay contents calculated by our model fit the best with results from smear slide analysis. This study demonstrates that our double-solid-matrix model can be an effective tool to understand the effect of heterogeneously distributed hydrates on velocities, as well as obtain accurate hydrate content in marine isotropic sediments.

Key words: Microstructure; Numerical modelling; Downhole methods; Gas and hydrate systems.

1. INTRODUCTION

Gas hydrates are naturally occurring ice-like solids with widespread distribution in permafrost regions and offshore continental margins. Controversies exist regarding the global total mass estimations of methane locked inside its cage-like structure, but global hydrate is rather considerable even by conservative estimates (e.g. Boswell & Collett 2011; Ruppel 2018). Gas hydrate has been widely investigated due to its significance in relation to geohazards and its role in historical and potential future climate change. Human activities (e.g. petroleum and natural gas exploitation) or natural temperature variations in sea level or the earth's interior can potentially contribute to the hydrate dissociation (e.g. Ruppel & Kessler 2017), releasing methane, a greenhouse gas with significantly higher global warming potential than carbon dioxide, into the atmosphere (Ruppel & Waite 2020; Sahoo & Best 2021). On the other hand, gas hydrate provides valuable insights for the techniques related to carbon capture and storage (Yu *et al.* 2021), one promising solution to the carbon emission reduction. These factors have been attracting interest in understanding and quantifying gas hydrates.

Field evidence indicates that the microscopic shapes and arrangement of gas hydrate (i.e. morphology) in the host sediments are highly variable (Sloan & Koh 2008). Holland (2008) categorizes the hydrate morphologies into (i) hardly visible fluid-displacing

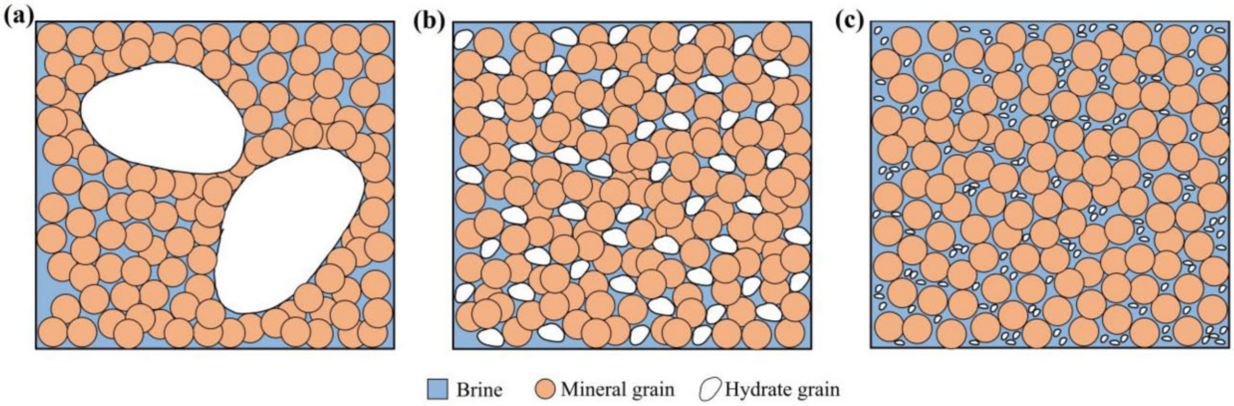

Figure 1. Conceptual diagrams (not to scale) showing the microstructure of isotropic sediment with the occurrence of (a) heterogeneously distributed hydrates, (b) matrix-supporting and (c) pore-floating hydrates. Matrix-supporting and pore-floating hydrates are two typical types of homogeneous distributed hydrates.

morphology (i.e. pore-filling) in coarse-grained sediments and (ii) visible grain-displacing type in fine-grained sediments, according to whether the hydrates displace the pore fluids or mineral grains during forming process. Further observations (e.g. Collett *et al.* 2009; Dai *et al.* 2012) show grain-displacing hydrate can exist as either (i) lenses or veins filling in the fractures or (ii) nodule and chunk-like hydrate in clay-rich sediments. Moreover, the fluid-displacing hydrate can be subdivided into cementing, matrix-supporting and pore-floating, depending on whether solid hydrate cements the sediment grains, bridges the minerals, or floats in the fluid without contact with solid components (Sahoo *et al.* 2018a; Pan *et al.* 2023).

Several rock physics models that consider homogeneous hydrate distributions in isotropic media have proven effective for permafrost or marine sediments. For example, the validity of contact-cementing theory (Dvorkin *et al.* 1994; Ecker *et al.* 1998), which assumes hydrate evenly coats on the sediment grain, has been demonstrated by Guerin *et al.* (1999) and Waite *et al.* (2004). Widely used matrix-supporting scheme (Dvorkin & Nur 1996) that considers fluid-displacing hydrate as part of the solid matrix has been validated by velocity measurements from various unconsolidated hydrate-bearing sediments (e.g. Wang *et al.* 2011; Kim *et al.* 2013; Pan *et al.* 2019). The pore-floating model, which assumes the fluid-displacing hydrate forms in the pore space away from grain contacts, has been verified by seismic data from Blake Ridge (Ecker *et al.* 1998) and experiments of Best *et al.* (2013). However, little attention has been paid to the influence of heterogeneously distributed hydrate on the *P*- and *S*-wave velocities, leading to uncertainties in hydrate saturation estimates. In this study we aim to address this gap by proposing a rock physics model for sediment with a heterogeneous hydrate distribution.

Elastic velocities of sediment hosting heterogeneously distributed hydrates depends on the corresponding hydrate formation mechanism. As shown by microstructure in Fig. 1(a), hydrate presents in the shapes ranging from spherical to oblate, as a result of the displacement of surrounding mineral grains in all directions during the formation process (Cook *et al.* 2008; Daigle & Dugan 2010). These heterogeneously distributed hydrates are (i) larger than sediment grains in scale and (ii) not perfectly uniformly mixed with the mineral grains. Consequently, rock is elastically isotropic, but its solid matrix is not as homogeneous as those in sediment hosting matrix-supporting and pore-floating hydrates (e.g. Figs 1b and c). In this case, the Voigt–Reuss–Hill average, a strictly heuristic theory used in matrix-supporting and pore-floating hydrate models (Helgerud *et al.* 1999), may not be applicable for modelling of heterogeneously distributed hydrates (Brown & Korringa 1975; Mavko *et al.* 1998; Dvorkin *et al.* 2007).

In this study, we propose a double-solid-matrix model based on the theory of Berryman and Milton (Berryman & Milton 1991) to predict the velocities of isotropic sediment hosting heterogeneously distributed hydrates. Using the proposed model we investigate the effect of important petrophysical properties on the velocities of heterogeneous-hydrate-bearing sediments. Then we compare the velocities simulated by the proposed scheme and two existing rock physics models designed for homogeneous distributed hydrates. Downhole measurements (e.g. resistivity, gamma ray, chloride concentration and smear slide of core samples) at Site 1245 from Ocean Drilling Programme (ODP) Leg 204 and Site U1328 from International Ocean Drilling Programme (IODP) Expedition 311 are used to evaluate the model capability.

2. DOUBLE-SOLID-MATRIX MODEL

Two schemes can provide insights for elastic modelling of isotropic sediment hosting heterogeneously distributed hydrates: (i) the composite Gassmann model (Gurevich & Carcione 2000), which provides the moduli of saturated composite rock by applying a particular mixing law on moduli of individual saturated solid phase and (ii) the model of Brown & Korringa (1975), which rigorously extend Gassmann's equations to allow for an isotropic medium with non-uniform-mixed solid components. Based on Brown and Korringa's equations, Berryman & Milton (1991) further derived exact formulas for the composite media with two homogeneous porous phases (e.g. sediment shown in Fig. 1a). Furthermore, theoretical simulations by Gurevich & Carcione (2000) indicated that Berryman and Milton's model is more applicable than the composite Gassmann model in the case where fluid flows between two homogeneous solid phases. Because fluid may flow between the pore space of sediment grains and possible micropores inside the hydrate (Marín-Moreno *et al.* 2017; Sahoo *et al.* 2018a), in this work we employ Berryman and Milton's theory for modelling of sediment hosting heterogeneously distributed hydrates.

For rocks with microscopically heterogeneous solid components, Brown & Korringa (1975) proposed to compute the elastic properties by a rigorous scheme involving four important bulk moduli: (i) dry composite solid matrix modulus, K^*_{dry}, (ii) composite solid grain modulus, K_s^*, (iii) pore space modulus, K_ϕ^* and (iv) fluid modulus, K_f. Of these four moduli, K_f can be computed using Reuss bound (Reuss 1929) and K_ϕ^* can be obtained using K_{dry}^* and K_s^* (Brown & Korringa 1975). In a composite porous medium with two solid matrices, either K_s^* or K_{dry}^* can be calculated from the other according to Berryman & Milton (1991). K_{dry}^* can be calculated using the bulk moduli of two solid matrices when the two phases are the same in shear modulus (e.g. Hill 1963). However, for sediment hosting heterogeneously distributed hydrates, hydrate and mineral phases are distinct in shear modulus. As a result, either K_{dry}^* or K_s^* is required to be known to calculate elastic properties using Brown & Korringa (1975) and Berryman & Milton (1991) models.

We propose following steps to obtain the elastic properties of sediment hosting heterogeneously distributed gas hydrates. We assume the solid matrix is composed of two parts (Fig. 1a), hydrate matrix (i.e. the matrix composed of gas hydrates) and mineral matrix (i.e. the matrix composed of mineral grains), and the region occupied by each matrix is big enough to have well-defined moduli. Then the bulk and shear moduli of the composite of these two matrices K_{dry}^* and G_{dry}^* can be obtained by a mixing law, Hashin–Shtrikman lower bound. Using this determined K_{dry}^*, we can derive K_s^* according to Berryman & Milton (1991). Finally, the velocities of saturated composite material can be computed using the generalized Gassmann equation (Brown & Korringa 1975).

2.1. Dry mineral matrix

Porosities within hydrate and mineral phases are usually variable during the hydrate formation process, which is vital for the rock physics modelling. Growing hydrate in the fine-grain medium always compacts the surrounding unconsolidated sediment due to the nature of hydrate formation (Spangenberg 2001; Jain & Juanes 2009). We do not consider the porous structure within pure hydrate, as the porosity within hydrate is not well-understood (see details in Discussion). In this case, the accumulation of hydrate would lower the porosity of the mineral matrix $\phi_{\text{min eral}}$ (the ratio of the volume of mineral grains to the saturated mineral matrix) from initial porosity ϕ_{initial} (sediment porosity prior to the hydrate presence, which is usually estimated from density log) to

$$\phi_{\text{min eral}} = \frac{\phi_{\text{initial}}(1 - S_{gh})}{1 - \phi_{\text{initial}} S_{gh}}, \tag{1}$$

where S_{gh} is the hydrate saturation (the ratio of the hydrate volume to the total pore space).

Various Hertz-theory-based effective medium models for hydrate-bearing unconsolidated sediment are incomplete as the solid grains are assumed to be infinitely rough only (e.g. Dvorkin & Nur 1996 model; Helgerud *et al.* 1999 model). Recently, a unified effective medium theory by Terry & Knapp (2018) has extended those traditional one-side models to the situation where rough and smooth spheres coexist, and has proven effective for unconsolidated sediments (e.g. Zhu *et al.* 2023). Here we employ this model to compute the bulk and shear moduli of dry mineral matrix, K_{dry1} and G_{dry1}. The moduli at critical porosity are given by

$$G_{dry1} = G_{HM} = \frac{[2 - \upsilon + 3\alpha(1 - \upsilon)]}{5(2 - \upsilon)} \left[\frac{3{G_{s1}}^2 n^2 (1 - \phi_c)^2}{2\pi^2 (1 - \upsilon)^2} P \right]^{\frac{1}{3}}, \tag{2}$$

$$K_{dry1} = K_{HM} = \left[\frac{{G_{s1}}^2 n^2 (1 - \phi_c)^2}{18\pi^2 (1 - \upsilon)^2} P \right]^{\frac{1}{3}}, \tag{3}$$

$$\upsilon = \frac{0.5(K_{s1} - \frac{2}{3} G_{s1})}{(K_{s1} + \frac{1}{3} G_{s1})}, \tag{4}$$

where K_{HM} and G_{HM} are moduli in the 'extended' Hertz–Mindlin effective medium model. ϕ_c, n, υ are the critical porosity, coordination number and poisson ratio, respectively. α represents the friction coefficient describing the strength of the transverse stiffness for particle contact (Jenkins *et al.* 2005). Two end states, the infinitely smooth and perfect stick grains (i.e. no-slip), occur when α equals 0 and 1, respectively. Voigt–Reuss–Hill average (Mavko *et al.* 1998) is usually used to compute solid moduli K_{s1} and G_{s1}. P is effective pressure accounting for the difference between lithostatic and hydrostatic pressure (Helgerud *et al.* 1999)

$$P = (\rho_b - \rho_w) g d, \tag{5}$$

where ρ_b and ρ_w are sediment bulk density and water density, respectively; g is the gravitational acceleration; and d is the depth (meters below sea floor) of sediment. K_{dry1} and G_{dry1} for sediment with mineral matrix porosity $\phi_{\text{min eral}}$ below or above ϕ_c are extended by Dvorkin *et al.* (1999).

2.2. Dry composite matrix

For a solid matrix composed of two isotropic granular porous materials but with unknown geometries of grains and pores, its effective moduli would fall between the two narrowest ranges, the lower and upper Hashin–Shtrikman bounds (Hashin & Shtrikman 1963). The two bounds are computed by simply arranging the two solid matrices as double homocentric spheres; the lower bound can be physically interpreted as the case where the inner sphere is the stiffer material, while the upper bound is realized when the stiffer sphere is the shell. In the case of sediment hosting heterogeneously distributed hydrates, given that hydrate is embedded in surrounding mineral grains (Fig. 1a), we simplify the structure of solid grains as two homocentric spheres, in which the hydrate matrix and softer mineral matrix constitute the inner and outer sphere packs, respectively (Liu *et al.* 2022). Therefore, the lower Hashin–Shtrikman bound can be used to obtain the moduli of a dry composite matrix, K_{dry}^* and G_{dry}^*:

$$K_{dry}^* = K_{dry1} + \frac{f_2}{(K_{dry2} - K_{dry1})^{-1} + f_1 (K_{dry1} + 4G_{dry1}/3)}, \tag{6}$$

$$G_{dry}^* = G_{dry1} + \frac{f_2}{(G_{dry2} - G_{dry1})^{-1} + \frac{2f_1(K_{dry1} + 2G_{dry1})}{5G_{dry1}(K_{dry1} + 4G_{dry1}/3)}}, \tag{7}$$

where f_1 and f_2 represent the mineral and hydrate proportions in the composite solid matrix, respectively. K_{dry2} and G_{dry2} are bulk and shear moduli of the hydrate matrix. Since we assumed a non-porous hydrate in Section 2.1, the moduli of the hydrate matrix are the same as the moduli of hydrate ($K_{dry2} = K_{s2}$, $G_{dry2} = G_{s2}$).

2.3. Saturated rock

For sediment hosting heterogeneously distributed hydrates, the original fluid substitution theory (Gassmann 1951) can be no longer applicable as it assumes either only one solid constituent or a composite matrix with uniformly mixed solid components. Brown & Korringa (1975) extended Gassmann's theory to the case of the

Table 1. Fixed parameters involved in the elastic rock physics modelling.

Constituent	K(Gpa)	G(Gpa)	ρ(g cm^{-3})	Source
Quartz	38.4	44.1	2.66	Pabst & Gregorová (2013)
Clay	20.9	6.85	2.58	Helgerud *et al.* (1999)
Hydrate	8.3	3.54	0.924	Helgerud *et al.* (2009)
Water	2.3	0	1.02	Cook & Waite (2018)

Table 2. Case-dependent parameters used in the elastic rock physics modelling.

Parameter	Symbol	Unit	Value
Bulk moduli			
Composite solid grains	K_s^*	Pa	Given in eq. (8)
Dry composite matrix	K_{dry}^*		Given in eq. (6)
Dry mineral matrix	K_{dry1}		Given in eq. (3)
Dry hydrate matrix	K_{dry2}		Hydrate bulk modulus (in Table 1)
Mineral grain	K_{s1}		Calculated using Voigt–Reuss–Hill average (Mavko *et al.* 1998)
Hydrate	K_{s2}		Hydrate bulk modulus (in Table 1)
Pore space	K_ϕ^*		Given in eq. (12)
Fluid content	K_f		Calculated using Reuss bound (Mavko *et al.* 1998)
Shear moduli			
Dry composite matrix	G_{dry}^*	Pa	Given in eq. (7)
Dry mineral matrix	G_{dry1}		Given in eq. (2)
Dry hydrate matrix	G_{dry2}		Hydrate shear modulus (in Table 1)
Mineral grain	G_{s1}		Calculated using Voigt–Reuss–Hill average (Mavko *et al.* 1998)
Hydrate	G_{s2}		Hydrate shear modulus (in Table 1)
Porosities			
Mineral matrix	$\phi_{min\,eral}$	Unitless	Given in eq. (1)
Initial porosity	$\phi_{initial}$		Estimated from density logs
Critical porosity	ϕ_c		0.37 (Guerin *et al.* 2006)
Friction coefficient	α	Unitless	0.1 (Site U1328)
			0.25 (Site 1245)
Coordination number	n	Unitless	9 (Guerin *et al.* 2006)
Effective pressure	P	Pa	Given in eq. (5)

heterogeneous solid matrix, but their result contains two new compressibilities (i.e. K_s^* and K_ϕ^*,) that need to be known. Here we determine the K_s^* and K_ϕ^* by adopting the idea of Berryman & Milton (1991): assuming a uniform swelling or shrinking in the composite rock (i.e. shapes and relative positions of hydrate matrix and mineral matrix remain unchanged with the variation of overall rock size), then the K_s^* and K_ϕ^* can be calculated from K_{dry}^* (given in eq. 6), K_{dry1} (obtained from eq. 3) and K_{dry2} (shown in Table 1, 2).

The composite grain modulus K_s^* can be calculated by:

$$K_s^* = \frac{K_{dry}^*}{1 - \sigma^*}, \tag{8}$$

$$\sigma^* = \sigma_1 + \frac{K_{dry}^* - K_{dry1}}{K_{dry2} - K_{dry1}} \left(\sigma_2 - \sigma_1\right), \tag{9}$$

where σ_1 and σ_2 are two parameters defined as:

$$\sigma_1 {=} 1 - \frac{K_{dry1}}{K_{s1}}, \tag{10}$$

$$\sigma_2 {=} 1 - \frac{K_{dry2}}{K_{s2}}. \tag{11}$$

σ_2 equals 0 in this study since we assume the heterogeneously distributed hydrate is a non-porous inclusion within the host sediment. Once K_s^* is determined, the effective modulus for pore space, K_ϕ^*, can be computed by:

$$K_\phi^* = \frac{\langle \phi \rangle}{\frac{\sigma^*}{K_s^*} - \left\langle \frac{\sigma(x) - \phi(x)}{K_s(x)} \right\rangle - \left(\langle \sigma(x) \rangle - \sigma^*\right) \left(\frac{\sigma_1 - \sigma_2}{K_{dry1} - K_{dry2}} \right)}, \tag{12}$$

where $\langle \cdot \rangle$ stands for the volume average of a material quantity, for example, $\langle q(x) \rangle = f^{(1)} q^{(1)} + f^{(2)} q^{(2)}$, $f^{(i)}$ denotes the volume fraction of the ith constituent.

Then the moduli of the saturated medium can be computed using the rearranged equation of Brown & Korringa (1975):

$$K_{sat} = K_{dry}^* + \sigma^* C, \tag{13}$$

$$G_{sat} = G_{dry}^*, \tag{14}$$

$$C = \frac{\sigma^*}{\sigma^*/K_s^* + \langle \phi \rangle \left(1/K_f - 1/K_\phi^*\right)}. \tag{15}$$

Velocities of compressional wave (V_P) and shear wave (V_S), and bulk density (ρ_b) can be obtained by:

$$V_p = \sqrt{\frac{K_{sat} + \frac{4}{3} G_{sat}}{\rho_b}}, \tag{16}$$

$$V_s = \sqrt{\frac{G_{sat}}{\rho_b}}, \tag{17}$$

$$\rho_b = \phi_{initial}(1 - S_{gh})\rho_f + \phi_{initial} S_{gh} \rho_{gh} + (1 - \phi_{initial})\rho_{mineral}, \tag{18}$$

where ρ_f, ρ_{gh} and $\rho_{mineral}$ represent the density of fluid (brine water), hydrate matrix and mineral matrix, respectively.

3. THEORETICAL VELOCITIES

Initial porosity, hydrate saturation and friction coefficient are significant parameters in our heterogeneous model. Fig. 2 shows their

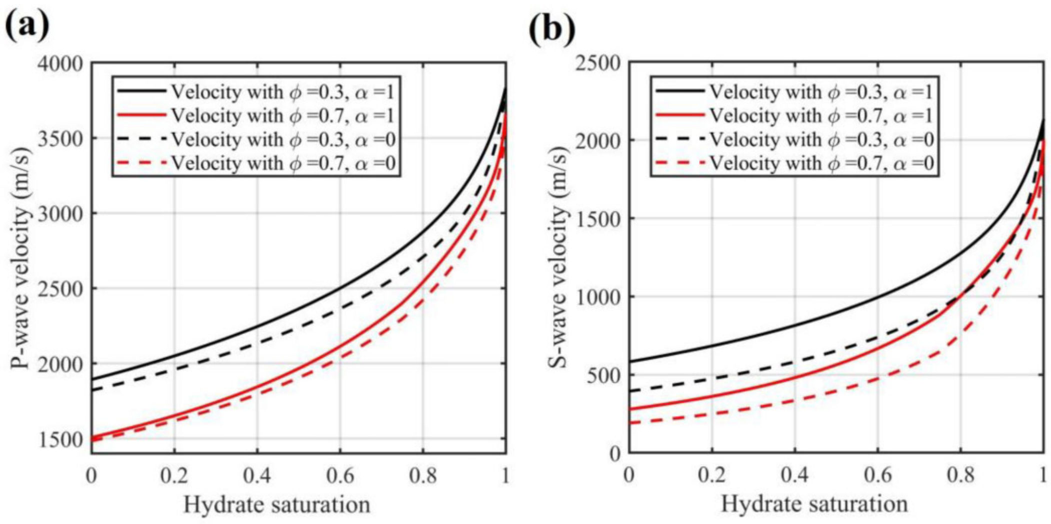

Figure 2. (a) *P*-wave velocity and (b) *S*-wave velocity of isotropic sediment hosting heterogeneously distributed hydrates as a function of hydrate saturation. Minerals constituting the sediment are 50 per cent clay and 50 per cent quartz. Water depth is 100 mbsf. Solid and dashed lines represent velocities estimated with a friction coefficient of 1 and 0, respectively.

effect on the velocity predictions. As shown, the presence of heterogeneously distributed gas hydrate significantly increases both *P*- and *S*-velocities, and the influence of hydrate accumulation on velocities become more significant as hydrate saturation increases. On the other hand, the increase in initial porosity lowers both *P*- and *S*-velocities, and the effect of porosity variation on velocities is less significant with the increase of hydrate saturation. Moreover, the increase in friction coefficient enhances the sediment velocities, and such velocity increase goes up when hydrate saturation is less than 70 per cent but decreases as hydrate saturation increases further.

Figs 3 and 4 compare the velocities simulated from our heterogeneous model and velocities predicted by matrix-supporting (Dvorkin & Nur 1996) and pore-floating models (Ecker *et al.* 1998), two existing models designed for homogeneous distributed hydrates. It should be noted that the widely used contact-cementing model (Dvorkin & Nur 1996), another homogeneous distribution mode, is not included in this velocity comparison. The reason is that contact-cementing model assumes a sediment porosity much lower than the critical porosity ranging from 36 to 40 per cent, whereas heterogeneously distributed hydrates are commonly observed in high-porosity (≥50 per cent) sediments (e.g. Tréhu *et al.* 2003).

A clear dependence of sediment velocities on rock physics models is illustrated in Figs 3 and 4. From Figs 3(d–f) and Figs 4(d–f), we find that V_S estimates from Models I–III are distinct in values. Of these three models, our heterogeneous model yields the highest V_S, followed by the matrix-supporting and pore-floating models. In the case of hydrate saturation lower than 70 per cent, V_S for our heterogeneous hydrate model increases more rapidly than V_S for the matrix-supporting model. However, as hydrate saturation increases further, V_S for our heterogeneous hydrate model increases much slower than the matrix-supporting model. From Figs 3 and 4 we also observe that V_P for our heterogeneous hydrate model is quite close to V_P for the matrix-supporting model. Apparent difference between V_P predictions from these two models can only be observed when host sediment is highly porous and hydrate-saturated (e.g. Figs 3c and 4c).

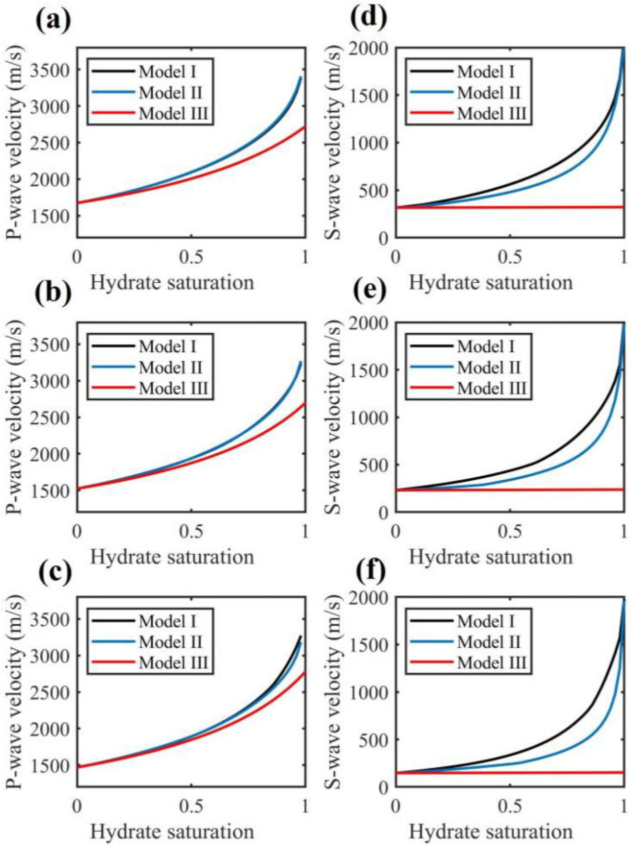

Figure 3. Comparison of *P*- and *S*-wave velocities calculated from Models I–III. Friction coefficient α is set to 0. (a–c) *P*-wave velocity estimated with a porosity of 40, 60 and 80 per cent, respectively. (d–f) *S*-wave velocity estimated with an initial porosity of 40, 60 and 80 per cent, respectively. Models I–III are our heterogeneous model, matrix-supporting model and pore-floating model, respectively. Minerals constituting the sediment are 50 per cent clay and 50 per cent quartz. Water depth is 100 mbsf.

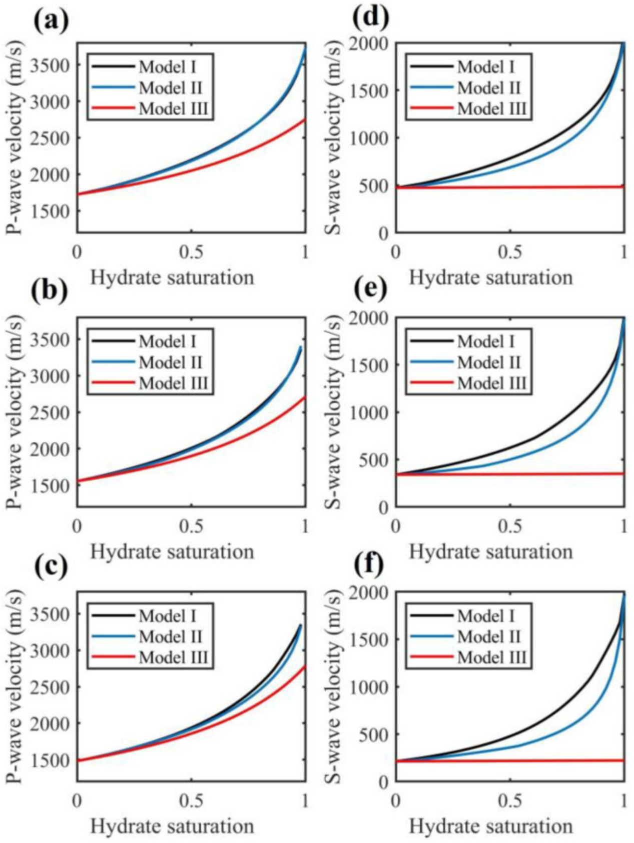

Figure 4. Comparison of *P*- and *S*-wave velocities calculated from Models I–III. Friction coefficient α is set to 1. (a–c) *P*-wave velocity estimated with a porosity of 40, 60 and 80 per cent, respectively. (d–f) *S*-wave velocity estimated with a porosity of 40, 60 and 80 per cent, respectively. Models I–III are our heterogeneous model, matrix-supporting model and pore-floating model, respectively. Minerals constituting the sediment are 50 per cent clay and 50 per cent quartz. Water depth is 100 mbsf.

4. APPLICATION TO NORTHERN AND SOUTHERN CASCADIA MARGIN

ODP Leg 204, the first drilling expedition dedicated to understanding gas hydrate formation processes in accretionary complexes with stratigraphically controlled gas conduits, has provided a testbed for techniques to depict hydrate occurrence in southern Cascadia margin (Tréhu *et al.* 2003, 2004). Physical properties measured from downhole logging devices during Leg 204 (Fig. 5) were employed to identify the hydrate accumulation and acquire hydrate volume within gas hydrate stability zone (GHSZ). Geochemical analyses of interstitial waters provided additional information on the hydrate distribution and concentration, the fluid migration within the GHSZ, and the rates of gas hydrate formation (Tréhu *et al.* 2003). Infrared (IR) imaging of core sample at Site 1245 has disclosed that hydrate, with a scale of a few centimetres, widely clusters above the bottom simulating reflector (BSR), especially within the interval 85–117 mbsf (meters below seafloor). At the same interval the measured resistivity is less than 2 Ωm, indicating sediments are isotropic and hydrates occupy the pore space instead of the fractures. In this study, the downhole measurements from this interval are used to assess the effectiveness of our model.

IODP Expedition 311 aimed to investigate the hydrate occurrences and their evolution along a transect located at the northern Cascadia accretionary margin. During this expedition a site, U1328, was established at a cold vent setting with active fluid and gas expulsion (Riedel *et al.* 2010). Drilling and coring were performed at this location to test the models for the cold vent structure and understand the cause of blanking zones on seismic data. Visual observations of gas hydrate during Expedition 311 were mostly from this cold venting site. Core samples from a hole, U1328C, indicated the presence of gas hydrate (Riedel *et al.* 2006; Hester *et al.* 2008). In the same hole pore water chlorinity and downhole resistivity measurements indicated the occurrence of abundant hydrates between 190 and 219 mbsf, as shown in Fig. 6. Resistivity measurements between 190 and 219 mbsf at Site U1328 indicated no presence of hydrate-filled fractures. Here we use downhole logs collected in this interval for model validation.

For models designed for isotropic hydrate-bearing sediments (models used in Fig. 4), coordination number n_p, critical porosity ϕ_c and the friction coefficient α are the site-specific constants that need to be determined for model applications. Given that n_p and ϕ_c at Sites U1328 and 1245 have been suggested by Guerin *et al.* (2006), here we just calibrate friction coefficient α at both sites. Friction coefficient is usually calibrated using the measured well-log data using the crossplots of *P*- and *S*-wave velocities versus hydrate saturation (e.g. Pan *et al.* 2020). Here we perform the calibration with the velocity measurements from hydrate-free intervals, to avoid the effect of errors from hydrate saturation estimates. For Site U1328 we use the velocity measurements in the interval from 97 to 104 mbsf, as both velocity and resistivity measurements indicated little or no hydrate. However, at Site 1245, hydrate-free intervals are hard to determine within depths above the BSR (about 130 mbsf), since IR scanning for core sections showed hydrates were widely present above the BSR (Guerin *et al.* 2006). In contrast, sediments beneath the BSR tend to be hydrate-free but are always linked with free gas. Here we calibrate the friction coefficient α for Site 1245 using the V_S measurements from 137 to 150 mbsf, given that resistivity indicated little gas only, and also, the effect of gas accumulation on V_S is negligible. Finally, α for Sites 1245 and U1328 are calibrated to be 0.25 and 0.1, respectively (Fig. 7). Note that we employ a 'background velocity' to describe the sediment velocity in the case of hydrate-free.

The assessment for an elastic rock physics model is generally performed by either (i) comparing the velocities from measurement and model prediction (e.g. Terry & Knapp 2018) or (ii) comparing the petrophysical properties from non-velocity measurement and model-based velocity inversion (e.g. Helgerud *et al.* 1999). We use both methods for this study and present the results in Sections 4.1 and 4.2.

4.1. Modelled velocities versus measured velocities

Non-velocity measurements can provide necessary petrophysical properties (e.g. sediment composition, hydrate saturation and sediment porosity) for rock physics models. Initial porosity, which are nearly unaffected by hydrate presence due to the comparability between hydrate and brine densities (Collett & Lee 2009), can be calculated from density logs. For host sediment at both sites, we assume it is a composite of sand and clay. In the case of clay content, we use an average of clay proportions from the smear slide within hydrate-bearing intervals (see Section 4.2.2). Additionally, hydrate saturation can be estimated from resistivity based on Archie's equation (Archie 1942); these saturation estimates depend on the saturation exponent *n* (Cook & Waite 2018), an empirical parameter highly related to hydrate distribution (Spangenberg 2001).

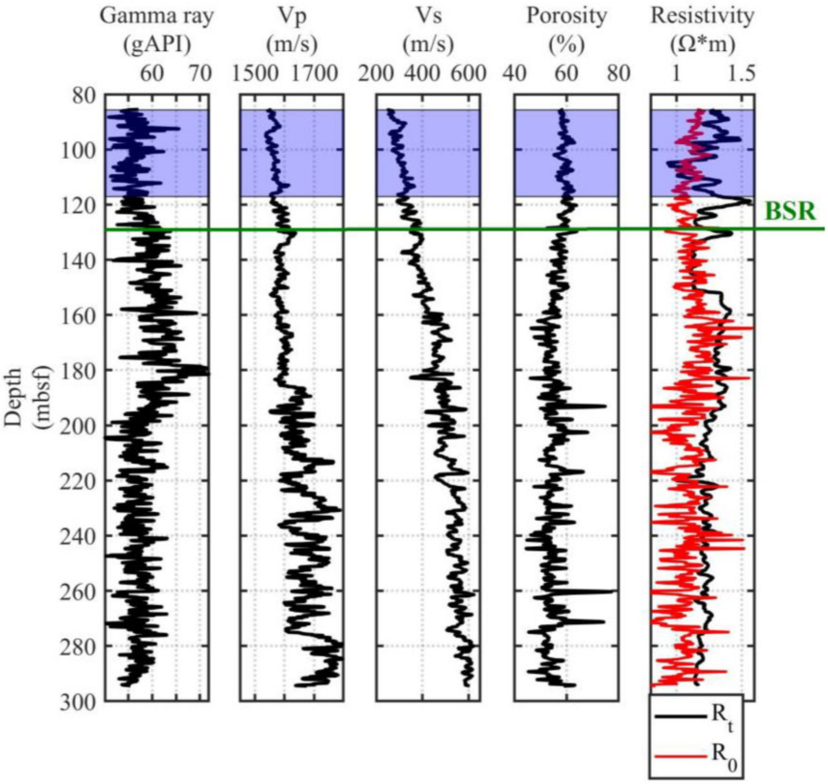

Figure 5. Gamma, velocity, porosity and resistivity logs collected at Site 1245E, ODP Leg 204. Blue shaded zone indicates the depth interval with the presence of hydrate. R_0 represents the calculated brine-saturated resistivity (see Section 4.3 for calculations).

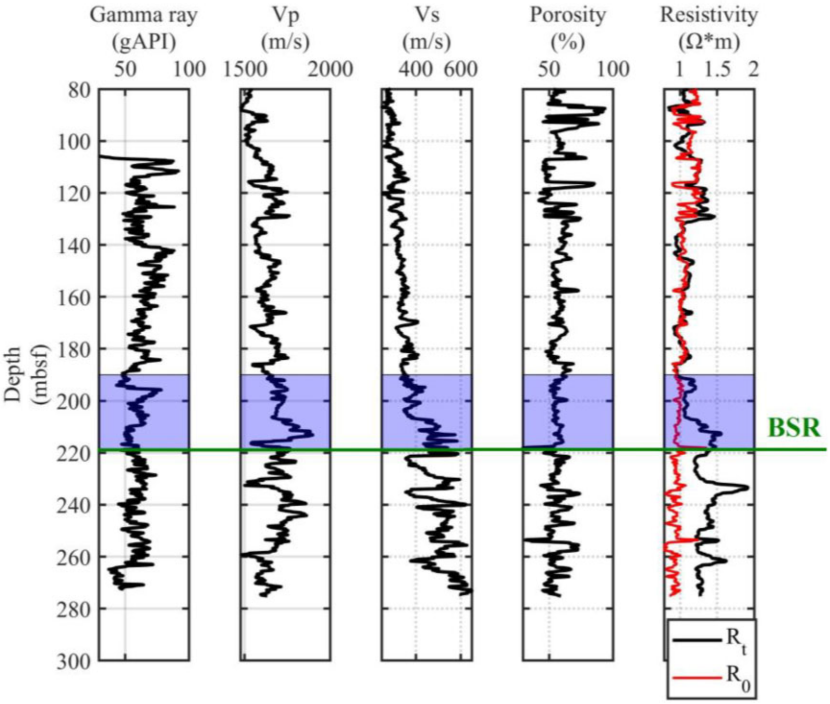

Figure 6. Gamma, velocity, porosity and resistivity logs collected at Site U1328C, IODP 311. Blue shaded zone indicates the depth interval with the presence of hydrate. R_0 represents the calculated brine-saturated resistivity (see Section 4.3 for calculations).

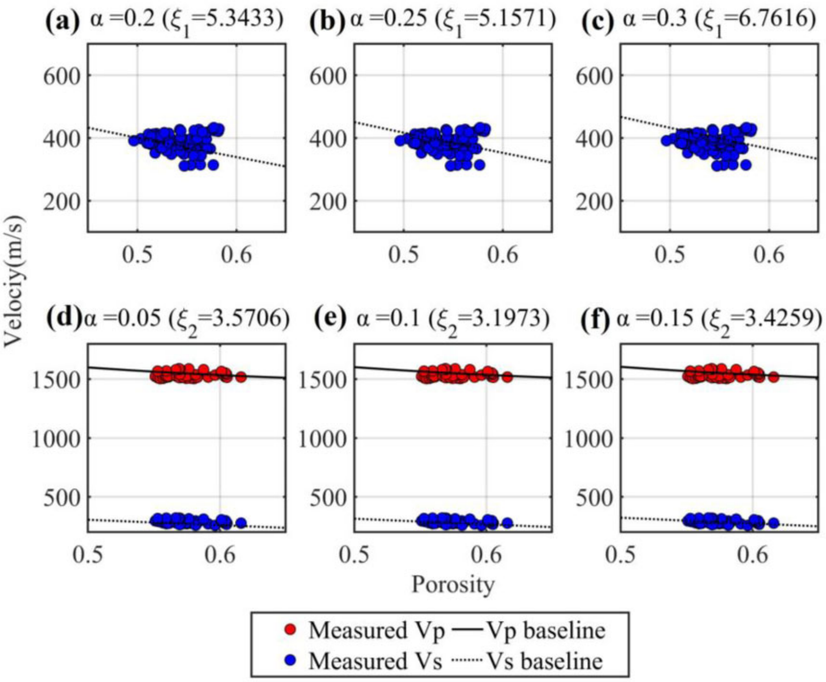

Figure 7. Measured velocities and modelled velocities using different friction coefficient α. Measured V_S at Site 1245E are plotted with the background V_S calculated with a α of (a) 0.2, (b) 0.25 and (c) 0.3. Measured V_P and V_S at Site U1328C are plotted with the background V_P and V_S calculated with a α of (d) 0.1, (e) 0.15 and (f) 0.2. Deviations between the measured and model-predicted background velocities in (a–c) and (d–f) are illustrated by ξ_1 ($\xi_1 = \sum_{i=1}^{N} \frac{|V_S^{\mathrm{est}}(i) - V_S^{\mathrm{meas}}(i)|}{V_S^{\mathrm{meas}}(i)}$) and ξ_2 ($\xi_2 = \sum_{i=1}^{N} (\frac{|V_P^{\mathrm{est}}(i) - V_P^{\mathrm{meas}}(i)|}{V_P^{\mathrm{meas}}(i)} + \frac{|V_S^{est}(i) - V_S^{\mathrm{meas}}(i)|}{V_S^{\mathrm{meas}}(i)})$), respectively. Clay content used in the baseline calculation is 60 per cent (Guerin *et al.* 2006).

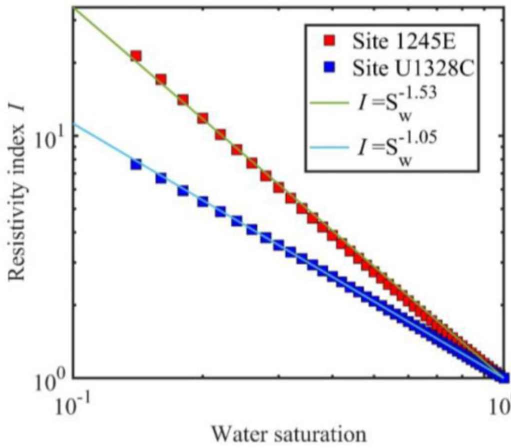

Figure 8. Crossplot of water saturation versus theoretical resistivity index for Sites 1245 and U1328.

However, to our knowledge, there is no available parameter n for the sediment hosting heterogeneously distributed hydrates.

Herein, we calibrate the saturation exponent n at both sites using an electrical model designed for heterogeneously distributed hydrates. First, we obtain the porosity exponent m from brine-saturated intervals according to Archie's law:

$$F = \frac{R_0}{R_w} = a\phi_{\mathrm{initial}}^{-m}, \tag{19}$$

where a is an empirical constant. R_0 is resistivity for brine-saturated sediment. R_w is the pore water resistivity, which depends on temperature and salinity and is usually calculated according to Arp (1953). For Site U1328, we estimate the R_w using a pore water salinity of 33 parts per thousand and a seafloor temperature of 3.5 °C. A thermal gradient of 53.6 $^{\circ}\mathrm{C\ km}^{-1}$ is used to derive the temperature at a specific depth below the seafloor (Riedel *et al.* 2006). At Site 1245, R_w versus depth is derived using a pore water salinity of 35 parts per thousand, a seafloor temperature of 4 °C, and a thermal gradient of 54.6 $^{\circ}\mathrm{C\ km}^{-1}$ (Tréhu *et al.* 2003). Porosity exponents $m = 1.70$ and $m = 0.87$ are determined for Sites 1245 and U1328, respectively. We show the estimated R_0 for all depths in Figs 5 and 6. Assuming that the gas hydrate grows in the shape of a sphere within a cubic host solid matrix, we can model the resistivity index I as a function of hydrate saturation (Spangenberg 2001)

$$I = \frac{\hat{F}\,\phi_{\mathrm{initial}}^{m}}{\left(\frac{\phi_{\mathrm{initial}}^{m}(1-S_{\mathrm{gh}})}{1-\phi_{\mathrm{initial}}^{m}S_{\mathrm{gh}}}\right)^{m}}, \tag{20}$$

where $\hat{F}$ is the effective formation factor depending on the hydrate saturation and growth pattern of hydrates. We then employ eq. (20) to calculate the I for sediment with S_{gh} ranging from 0 to 100 per cent. Based on the Archie's second law $I = (1 - S_{\mathrm{gh}})^{-n}$, we determined theoretical saturation exponents $n = 1.53$ and $n = 1.05$ for Sites 1245 and U1328, respectively (see Fig. 8). Finally the hydrate saturation within *in situ* hydrate-bearing sediment can be estimated from measured resistivity R_t with the rearranged Archie's second law:

$$S_{\mathrm{gh}} = 1 - \left(\frac{R_0}{R_t}\right)^{\frac{1}{n}}. \tag{21}$$

These resistivity-derived S_{gh} are used to compute the V_P and V_S through rock physics models shown in Figs 3 and 4. Fig. 9 displays the P- and S-wave velocity estimates and downhole velocity

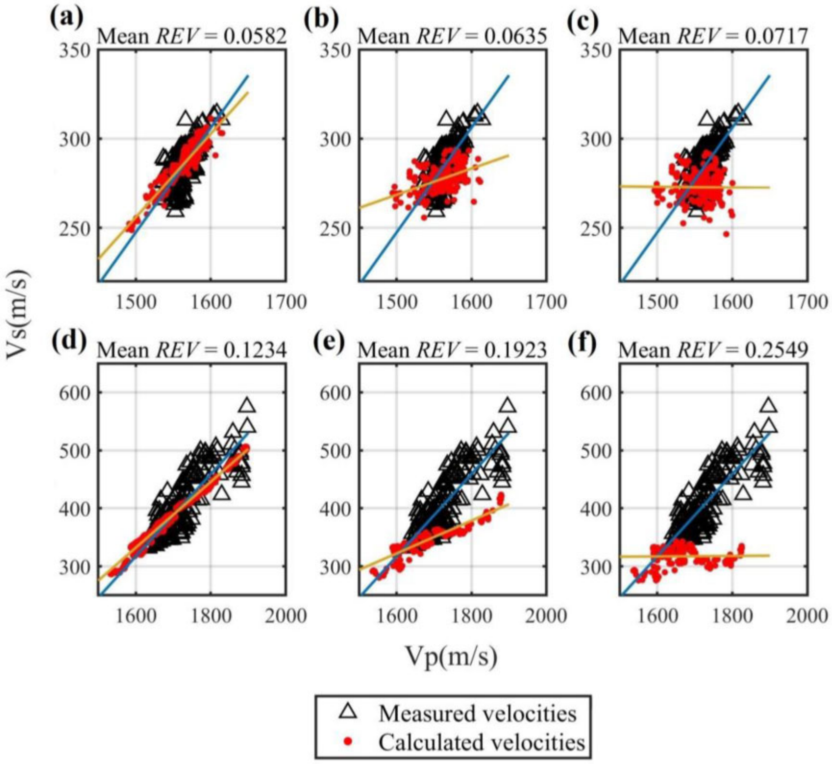

Figure 9. V_P and V_S from measurement and model estimation. Panels (a)–(c) are results for Site 1245, ODP 204 and panels (d)–(f) are results for Site U1328, IODP311. Rock physics models used in panels (a) and (d), (b) and (e) and (c) and (f) are our heterogeneous model, matrix-supporting model, and pore-floating model, respectively. Average clay proportions from smear slide analysis (see Section 4.2.2), 74.6 and 69.5 per cent, are used to calculate the velocity predictions for Sites 1245 and U1328, respectively. Mean REV is defined as average REV per sample point. Two lines indicate the linear regression trends for measured velocities and calculated velocities.

measurements at Sites 1245 and U1328. In order to depict the deviation between measured and modelled velocities, we introduce a relative error of velocities (REV)

$$\mathrm{REV} = \frac{\left|V_P^{\mathrm{est}} - V_P^{\mathrm{meas}}\right|}{V_P^{\mathrm{meas}}} + \frac{\left|V_S^{\mathrm{est}} - V_S^{\mathrm{meas}}\right|}{V_S^{\mathrm{meas}}}, \tag{22}$$

where subscripts est and meas represent the velocities from model estimation and downhole measurement, respectively.

For Sites 1245 and U1328, Fig. 9 also shows that velocities predicted by our heterogeneous model yield the lowest mean REV among three models, indicating our model can characterize the elastic properties of these hydrate-bearing sediments better than other two models. Moreover, of the three models, the linear relationship between V_P and V_S estimated by our model shows the best agreement with the velocity correlations shown by measurements. In contrast, both matrix-supporting and pore-floating models underestimate the V_S.

4.2. Petrophysical properties from velocity and non-velocity measurements

We also employ matrix-supporting model, pore-floating model and our heterogeneous model to estimate two petrophysical properties, hydrate saturation S_{gh} and clay proportion C_v, from velocity data. Initial porosity for inversion is derived from density logs (see Section 4.1). For each depth point, we obtain the estimates of S_{gh} and C_v through minimizing the REV shown in eq. (22). These petrophysical properties estimated from velocity and non-velocity measurements are compared in following sections.

4.2.1. Hydrate saturation

A commonly used method to accurately estimate the hydrate saturation in marine sediments is the measurement of chloride content within the pore fluids (e.g. Froelich *et al.* 1995; Hesse 2003). Abnormally low value on the chloride concentration profile is usually used as an indicator of hydrate presence as the dissociation of gas hydrate can freshen the pore fluids during core recovery. This geochemical method was employed at Sites 1245, ODP 204 and U1328, IODP 311 to provide reliable volume estimates of gas hydrate within the GHSZ. Using the chloride concentration model of Yuan *et al.* (1996), we obtain the *in situ* hydrate content for Sites 1245 and U1328, which are up to 18 and 37 per cent, respectively (Fig. 10).

Fig. 11 illustrates the velocity-derived S_{gh} (Vel $- S_{gh}$) varies depending on the rock physics models. For both sites, Vel $- S_{gh}$ estimates from our heterogeneous model conform well with the S_{gh} derived from chloride concentration ($Cl - S_{gh}$), while Vel $- S_{gh}$ predicted by pore-floating model are much lower than $Cl - S_{gh}$. Matrix-supporting model appears to yield Vel $- S_{gh}$ comparable with $Cl - S_{gh}$, but it underestimates the S_{gh} at several depths, e.g. 88 mbsf at Site 1245 and 192 mbsf at Site U1328. Overall, our heterogeneous model gives better hydrate saturation predictions than other models.

4.2.2. Clay content

Smear slide sample emerges as a rapid, simple and cheap method to study marine sediments, for example, identifying sediment types and classifying sediments. This technique generally only requires a

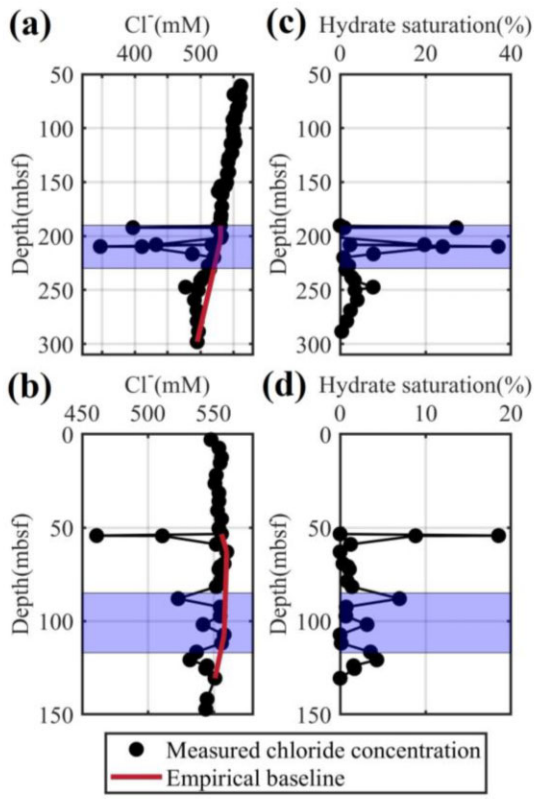

Figure 10. The chloride concentration profile at (a) Hole U1328C and (b) Hole 1245B and hydrate saturation derived from chloride anomalies at (c) Hole U1328C and (d) Hole 1245B. Highlighted zones indicate the hydrate-bearing intervals used in this work.

very small sample, making it possible to sample even archive cores without causing damage (Rothwell 1989). In Fig. 12, we present the clay proportions C_v derived from the smear slide and measured velocities at Sites 1245 and U1328. Moreover, in Fig. 12 we show the original gamma ray, a good indicator of clay content of the sediment, instead of the gamma-ray-derived C_v estimates, given that great uncertainties related to pure sand and shale baselines.

For Site 1245, Figs 12(a)–(c) show that clay contents predicted by all models appears to fit well with C_v from the smear slide. In addition, at the depth of 104 mbsf our heterogeneous model gives a better C_v prediction than matrix-supporting and pore-floating models. Overall, all models give close predictions to the results from gamma ray measurement in the interval from 90 to 110 mbsf. Clay contents beyond this interval seem to deviate from the trend indicated by gamma ray, which can be attributed to the presence of other lithologies in addition to clay and sand.

In the case of Site U1328, our heterogeneous model predicts the most consistent C_v estimates with those derived from smear slide, as indicated in Figs 12(d)–(f), whereas the other two models underestimate the clay content when compared to the smear slide results. Moreover, the clay content estimated using our heterogeneous model show a more agreement with gamma ray measurements than results from other two models. However, at depths between 210 and 215 mbsf, C_v values from all three models are much lower than the smear slide results; the variation of C_v values from all three models are not consistent with the clay content trend indicated by gamma ray log. The possible coexistence of hydrate and free gas, as illustrated by Riedel *et al.* (2006), could be the reason for such discrepancy.

5. DISCUSSION

5.1. Dependence of velocities on the hydrate morphologies

For velocity predictions from rock physics models (Fig. 3), the reason that *P*- and *S*-wave velocity for heterogeneously distributed hydrate-bearing sediments is higher than pore-filling hydrate-bearing sediment is the difference on the contribution to the rock rigidity: heterogeneously distributed hydrate within the pore space can support the solid frame and significantly increase the rigidity of the rock, whereas pore-filling hydrates floating within the pore fluid increase the fluid bulk modulus but do not contribute to the moduli of the dry rock. In addition, the reason that velocities (especially the *S*-wave velocity) for heterogeneously distributed hydrate-bearing sediments is higher than matrix-supporting hydrate-bearing sediment can be the sediment compaction resulting from hydrate formation. The growing heterogeneously distributed hydrates usually displace the mineral grains, compacting the host sediment, while matrix-supporting hydrates only occupy the pore space and hardly affect the arrangement of the mineral grains.

5.2. Heterogeneously distributed hydrates and nodule-like hydrates in isotropic sediments

Nodule-like hydrates in isotropic sediments (e.g. Fig. 13), tend to be larger than sediment grains in scale, appear to have the same microstructure with the heterogeneously distributed hydrates (see Fig. 1a). Moreover, the depths with the presence of nodule hydrates at Sites 1245 and U1328, as observed by naked eyes and core scanning techniques (Tréhu *et al.* 2003; Riedel *et al.* 2006), are within the intervals where velocities predicted by our double-matrix-model match well with the velocity measurements. In this case, the natural nodule-like hydrates deposited in marine sediments are likely the heterogeneously distributed hydrates discussed in this work, and our double-matrix model may be used to predict the elastic properties of *in situ* sediments containing such nodule-like hydrates.

For nodule-like hydrate and non-nodule-like hydrate (i.e. vein-like or pore-filling hydrate), their different appearances could be primarily governed by the effective stress, often associated with buried depth and sediment grain size (Dai *et al.* 2012; Terzariol *et al.* 2020). We illustrate their formation mechanism in Fig. 14. For coarse-grained sediment, the large grain size (e.g. Fig. 14a) results in the ‘expanding’ capillary pressure (pressure difference between hydrate and water surfaces) being lower than the ‘compacting’ effective stress. Moreover, coarse sediments are highly permeable, allowing for the easy creation of gas flow (Collett 2001). Consequently, hydrate could readily grow within the pore space of the loosely packed sediment, which is known as pore-filling hydrate (e.g. Fig. 14d). In contrast, in muddy fine-grained sediment (e.g. Fig. 14b) capillarity force is much higher due to the smaller particle radius (Jain & Juanes 2009). Also creating gas flow paths in these low-permeability sediments is challenging (Collett 2001). As a result, hydrate can no longer invade through the pore throat but instead pushes sediment grains apart, that is, grain-displacing hydrate. An analogy can be drawn to a fracture-opening mechanism of gas invasion (Jain & Juanes 2009). Furthermore, when the lateral and vertical stresses within sediment are comparable, the grain

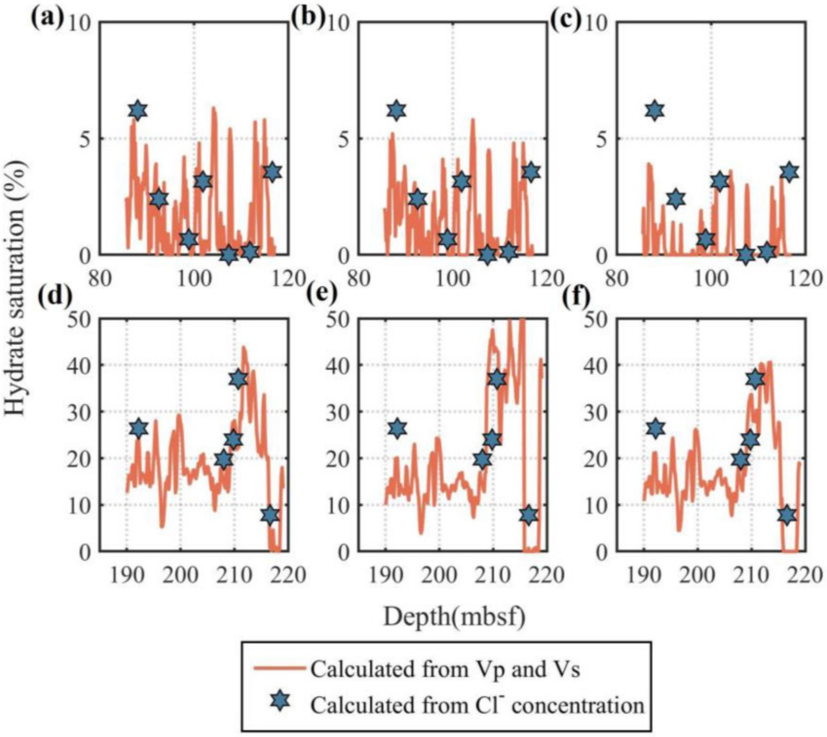

Figure 11. Hydrate saturations estimated from chloride concentration and velocity measurements. Panels (a)–(c) are results for Site 1245, ODP 204, and (d)–(f) are results for Site U1328, IODP311. Rock physics models used in panels (a) and (d), (b) and (e) and (c) and (f) are our heterogeneous model, matrix-supporting model, and pore-floating model, respectively.

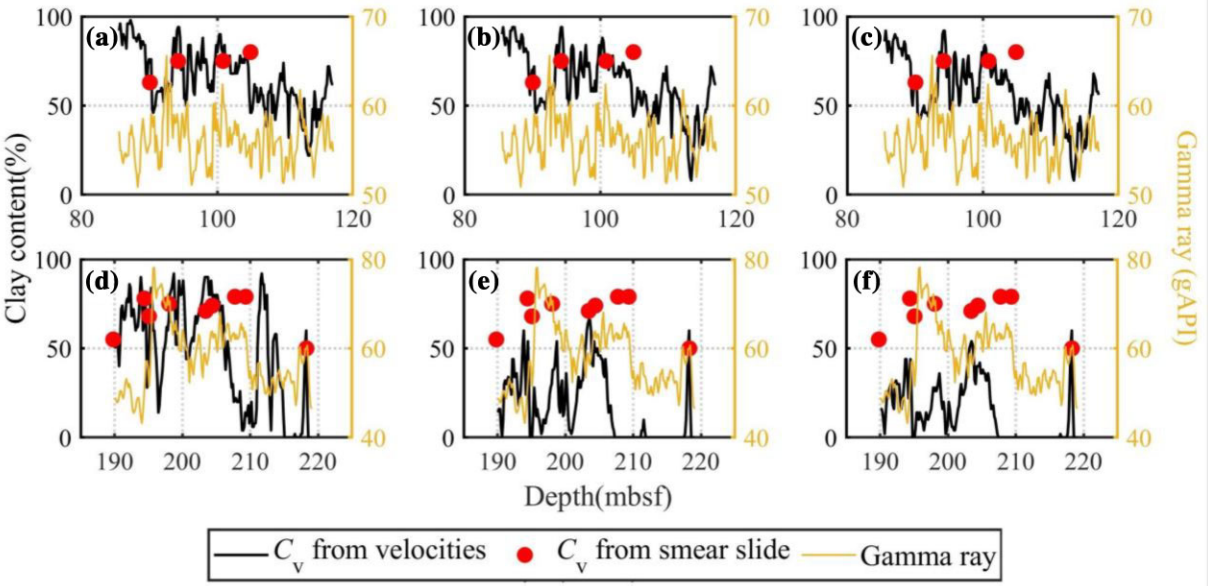

Figure 12. Gamma ray measurements and the clay proportions estimated from velocities and smear slide. Panels (a)–(c) are results for Site 1245, ODP 204, and (d)–(f) are results for Site U1328, IODP311. Rock physics models used in panels (a) and (d), (b) and (e), and (c) and (f) are our heterogeneous model, matrix-supporting model and pore-floating model, respectively.

displacement would occur in every direction, leading to nodule and chunk-shaped gas hydrate (e.g. Fig. 14e). However, within finer sediments (e.g. Fig. 14c), hydrates will present as veins shown in Fig. 14(f) if they find a low one directional stress path like fractures. Subvertical hydrate-filled veins observed in sediments with high-effective pressure can be a good illustration (e.g. Cook *et al.* 2008).

5.3. Applicability of double-solid-matrix model

Porous structure within the gas hydrate has been observed within natural gas hydrate aggregates (e.g. Kuhs *et al.* 2004; Sultan *et al.* 2014). In that case, our double-solid-matrix model remains useful as the elastic moduli are derived based on the model of Berryman

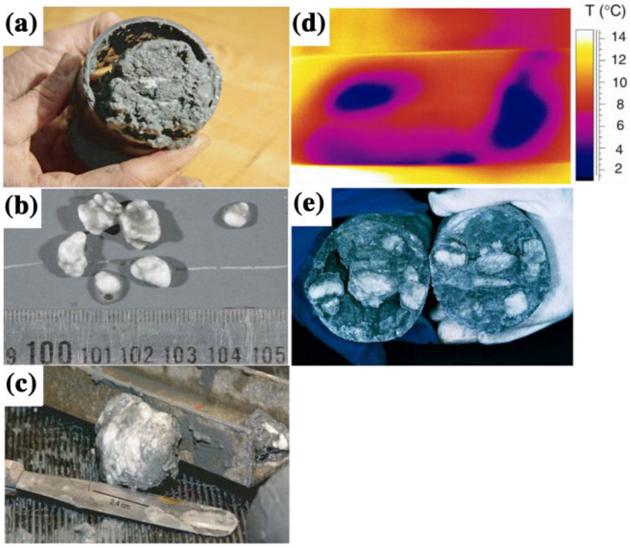

Figure 13. Nodule-like hydrates in the core samples. Panels (a–c) are images of gas hydrate samples recovered at Site U1328 during IODP 311 (modified from Riedel *et al.* 2006). Panels (d) and (e) depict the infrared images and hydrate samples extracted from the core liner during ODP Leg 204, respectively (modified from Tréhu *et al.* 2003).

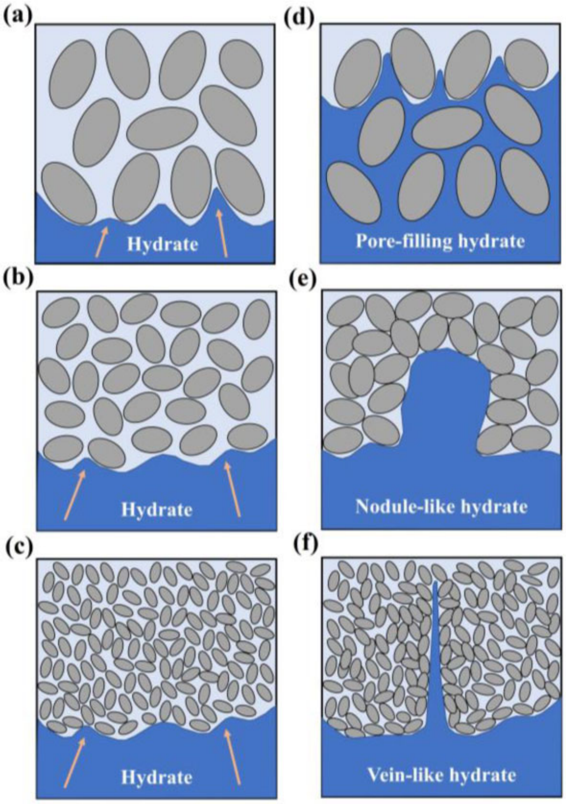

Figure 14. Conceptual diagrams (not to scale) showing the formation of hydrate in three morphologies. Panels (a) and (c) depict the sediment microstructure before and after invasion of pore-filling hydrate, respectively. Panels (b) and (e) illustrate the sediment microstructure before and after invasion of nodule-like hydrate, respectively. Panels (c) and (f) show the sediment microstructure before and after invasion of vein-like hydrate, respectively.

& Milton (1991), which is rigorously designed for the heterogeneous medium composed of two porous phases. The reasons why we consider a zero porosity for pure hydrate in this study are (i) the porous natural heterogeneously distributed hydrates were only observed nearby the seafloor so far (e.g. Suess *et al.* 2001; Sultan *et al.* 2014) and (ii) hydrate porosity is hard to be determined as it should be a variable depending on a number of factors such as effective pressure and buried depth. Here we also investigate the effect of porous structure of hydrate on the *P*- and *S*-wave velocities. Since pure gas hydrate is more likely to present as a consolidated substance instead of a simply heaping (Stern *et al.* 2011; Liu *et al.* 2022), we employ a consolidated-material-based model provided by Pride (2003) to calculate the moduli of dry hydrate matrix, K_{dry2} and G_{dry2}. The equations are shown below

$$K_{\mathrm{dry2}} = K_{\mathrm{gh}} \frac{1-\phi_{\mathrm{gh}}}{1+c\phi_{\mathrm{gh}}}, \tag{23}$$

$$G_{\mathrm{dry2}} = G_{\mathrm{gh}} \frac{1-\phi_{\mathrm{gh}}}{1+3c\phi_{\mathrm{gh}}/2}, \tag{24}$$

where c is the consolidation parameter representing the consolidation degree of hydrate grains. ϕ_{gh} is the porosity of hydrate matrix and usually ranges from 25 to 40 per cent (e.g. Kuhs *et al.* 2000; Stern *et al.* 2011).

Using the eqs (23) and (24) and double-solid-matrix model proposed in Section 2, we obtain the velocities for sediment hosting heterogeneously distributed hydrates under different hydrate matrix porosity and consolidation parameter conditions. As shown in Fig. 15, the increase of hydrate matrix porosity or the decrease of consolidation parameter can elevate the *P*- and *S*-wave velocities, as well as the velocities for the hydrate-saturated case (i.e. the maximum hydrate saturation). We speculate the reason for that can be the increment of fluid flow between hydrate and mineral porous phases: either the increase of hydrate matrix porosity or the decrease of consolidation parameter can stimulate the fluid flow between two porous solid phases.

Given that heterogeneously distributed hydrates are macroscopic solids embedded in the sediment, we regard the hydrate to be a solid matrix independent from the mineral grains. We assume that heterogeneity within the mineral matrix (multimineral grains) is negligible to that between the hydrate and mineral matrices, and then model the elastic properties of this heterogeneous isotropic medium based on Berryman and Milton's theory. However, when the mixture of mineral grains is uniform enough so that the regions occupied by individual minerals are comparable with the size of hydrate patches, mineral components should be seen as different solid matrices. In this case, the model of Berryman & Milton (1991) and our double-solid-matrix scheme are no longer suitable.

Although hydrates have been widely observed to be heterogeneously distributed during NGHP01 (Stern & Lorenson 2014), ODP Leg 204 (Tréhu *et al.* 2003), IODP 311 (Hester *et al.* 2008), GMGS2 (Zhang *et al.* 2015) and shallow methane hydrate research by the Ministry of Economy, Trade and Industry, Japan (Yoneda *et al.* 2019), researches also show that these heterogeneous hydrates can coexist with other hydrate morphologies at the same depth, for example, vein-like hydrates discovered by Lee & Collett (2009) and Tréhu *et al.* (2003). In these cases, hydrate can be quantified using a unified framework by integrating our double-solid-matrix model and other morphology-dependent models (e.g. Pan *et al.* 2022a, b).

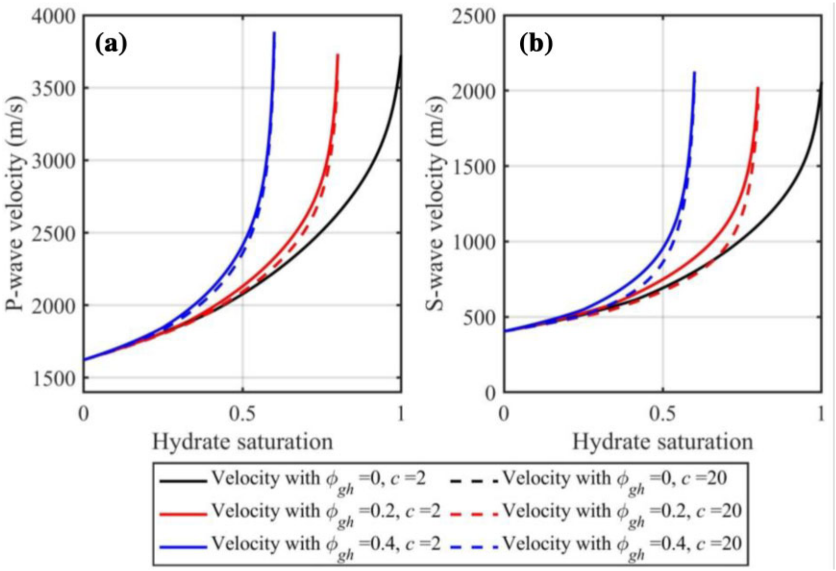

Figure 15. Velocities of isotropic sediment hosting heterogeneously distributed hydrates for various hydrate matrix porosity and consolidation parameter. (a) *P*-wave velocity and (b) *S*-wave velocity. Minerals constituting the sediment are 50 per cent clay and 50 per cent quartz. Water depth and friction coefficient is 100 mbsf and 1, respectively. Solid and dashed lines represent velocities estimated with a *c* of 2 and 20, respectively.

5.4. Uncertainties of hydrate saturations from non-velocity measurements

It should be noted that uncertainties may come from the use of improper parameters in Archie's equations. For instance, the determination of Archie parameters *a* and *m* can be somewhat subjective (Janik *et al.* 2009). Moreover, in Section 4.1 we propose a new scheme to calculate a proper saturation exponent *n* for sediment hosting heterogeneous hydrates, but more laboratory measurements are required to testify these *n* estimates. On the other hand, the effect of clay on the electrical resistivity was ignored when obtaining the hydrate saturation. As a result of the surface conduction by clay particles, *in situ* rock resistivity for shaley sandstone could be slightly lower than the shale-free sandstone (Sahoo *et al.* 2018b), which can yield a slightly underestimated hydrate saturation in Section 4.1.

Reference hydrate concentrations from chloride concentration measurements could be influenced by the uncertainty in estimating the background salinity (i.e. *in situ* fluid salinity prior to gas hydrate dissociation). Apart from gas hydrate formation, various geochemical processes, including clay dehydration, can result in abnormally low salinity on the chloride profile (Torres *et al.* 2004). For example, at Site U1328, a smooth decrease in chloride concentration at hydrate-free intervals could be attributed to the potential release of fresh water caused by dehydration reactions. To mitigate the impact of non-hydrate factors, the chloride baseline used in this study is defined as the envelope of measurements instead of a constant.

6. CONCLUSIONS

Hydrates can displace the surrounding fine sediment grains and lead to the presence of shapes ranging from spherical to oblate. Sediments hosting these heterogeneously distributed hydrates are elastically isotropic, with a multicomponent solid matrix composed of minerals and hydrates. In this study, we design a double-solid-matrix model to describe the elastic properties of these isotropic hydrate-bearing sediments. Based on a comparison of our model with two existing models designed for homogeneous distributed hydrate, we draw the following conclusions:

(1) Numerical simulations show our heterogeneous hydrate model and existing matrix-supporting model are quite similar in *P*-wave velocity predictions, and apparent difference can only be observed when host sediment is highly porous and hydrate-saturated. However, *S*-wave velocities calculated from our heterogeneous hydrate model are much higher than matrix-supporting and pore-floating models.

(2) Applications indicate our heterogeneous hydrate model is more effective than matrix-supporting and pore-floating models in terms of characterizing the hydrate-bearing sediment at Site 1245, ODP 204 and Site U1245, IODP311. At both sites, the velocities predicted by our model show better agreement with the measured velocities; hydrate saturations and clay contents derived from our heterogeneous model also conform better with the estimates from pore water chlorinity and smear slide analysis, indicating that heterogenous distributed hydrate in isotropic media is likely to behave as a separate isotropic solid matrix at the scale of well logging.

ACKNOWLEDGMENTS

The research work was supported by the National Key R&D Program of China (Grant No. 2021YFC2800900) and the National Natural Science Funding (Grant No. 52474076). The authors are grateful to the crew and science party of the Ocean Drilling Programme Leg 204 and International Ocean Drilling Programme Expedition 311 for access to the downhole logs. XZ thanks Prof. Angus I. Best and Dr Sourav K. Sahoo for inviting him to be a Visiting PhD Student Fellow at National Oceanography Centre, Southampton, UK.

DATA AVAILABILITY

Downhole logs and used in this study can be accessed from https://mlp.ldeo.columbia.edu/logdb/scientific_ocean_drilling/result.

REFERENCES

Archie, G.E., 1942. The electrical resistivity log as an aid in determining some reservoir characteristics, *Trans. Am. Inst. Min. Metall. Eng.,* **146,** 54–62.

Arp, J.J., 1953. The effect of temperature on the density and electrical resistivity of sodium chloride solutions, *Trans. Am. Inst. Min. Metall. Pet. Eng.,* **198,** 327–330.

Berryman, J.G. & Milton, G.W., 1991. Exact results for generalized Gassmann's equations in composite porous media with two constituents, *Geophysics,* **56,** 1950–1960.

Best, A.I., Priest, J.A., Clayton, C.R.I. & Rees, E.V.L., 2013. The effect of methane hydrate morphology and water saturation on seismic wave attenuation in sand under shallow sub-seafloor conditions, *Earth planet. Sci. Lett.,* **368,** 78–87.

Boswell, R. & Collett, T.S., 2011. Current perspectives on gas hydrate resources, *Energy Environ. Sci.,* **4**(4), 1206–1215.

Brown, R. & Korringa, J., 1975. On the dependence of the elastic properties of a porous rock on the compressibility of the pore fluid, *Geophysics,* **40,** 608–616.

Collett, T.S., 2001. *Natural Gas Hydrates: Vast Resources, Uncertain Future*. U.S. Geological Survey.

Collett, T.S., Johnson, A.H., Knapp, C.C. & Boswell, R., 2009. Natural gas hydrates: a review, in *Natural Gas Hydrates—Energy Resource Potential and Associated Geologic Hazards,* Vol. **89,** pp. 146–219. eds, Collett, T., Johnson, A., Knapp, C. & Boswell, R., American Association of Petroleum Geologists

Cook, A.E., Goldberg, D. & Kleinberg, R.L., 2008. Fracture-controlled gas hydrate systems in the northern Gulf of Mexico, *Mar. Pet. Geol.,* **25,** 932–941.

Cook, A.E. & Waite, W.F., 2018. Archie's saturation exponent for natural gas hydrate in coarse-grained reservoirs, *J. Geophys. Res.: Solid Earth,* **123,** 2069–2089.

Dai, S., Santamarina, J.C., Waite, W.F. & Kneafsey, T.J., 2012. Hydrate morphology: physical properties of sands with patchy hydrate saturation, *J. geophys. Res.,* **117,** B11205.

Daigle, H. & Dugan, B., 2010. Origin and evolution of fracture-hosted methane hydrate deposits, *J. geophys. Res.,* **115,** B11103.

Dvorkin, J., Mavko, G. & Gurevich, B., 2007. Fluid substitution in shaley sediment using effective porosity, *Geophysics,* **72**(3), O1–O8.

Dvorkin, J. & Nur, A., 1996. Elasticity of high-porosity sandstones: theory for two North Sea data sets, *Geophysics,* **61,** 1363–1370.

Dvorkin, J., Nur, A. & Yin, H., 1994. Effective properties of cemented granular material, *Mech. Mater.,* **18,** 351–366.

Dvorkin, J., Prasad, M., Sakai, A. & Lavoie, D., 1999. Elasticity of marine sediments: rock physics modeling, *Geophys. Res. Lett.,* **26**(12), 1781–1784.

Ecker, C., Dvorkin, J. & Nur, A., 1998. Sediments with gas hydrates: internal structure from seismic AVO, *Geophysics,* **63**(5), 1659–1669.

Froelich, P.N., Kvenvolden, K.A., Torres, M.E., Waseda, A., Didyk, B.M. & Lorenson, T.D., 1995. Geochemical evidence for gas hydrate in sediment near the Chile triple junction, In *Proc. ODP, Sci. Results,* Vol. **141,** pp. 279–286, eds, Lewis, S.D., Behrmann, J.H., Musgrave, R.J. & Cande, S.C., Ocean Drilling Program, College Station, TX

Gassmann, F., 1951. Über die Elastizität poröser Medien, *Viertel. Naturforsch. Ges. Zürich,* **96,** 1–23.

Guerin, G., Goldberg, D.S. & Collett, T.S., 2006. Sonic velocities in an active gas hydrate system, Hydrate Ridge, In *Proc. ODP, Sci. Results,* Vol. **204,** pp. 1–38. eds, Tréhu, A.M., Bohrmann, G., Torres, M.E. & Colwell, F.S., Texas A&M University

Guerin, G., Goldberg, D.S. & Melster, A., 1999. Characterization of in situ elastic properties of gas hydrate-bearing sediments on the Blake Ridge, *J. geophys. Res.,* **104,** 17 781–17 795.

Gurevich, B. & Carcione, J.M., 2000. Gassmann modeling of acoustic properties of sand-clay mixtures, *Pure appl. Geophys.,* **157**(157), 811–827.

Hashin, Z. & Shtrikman, S., 1963. A variational approach to the elastic behavior of multiphase materials, *J. Mech. Phys. Solids,* **11,** 127–140.

Helgerud, M.B., Dvorkin, J., Nur, A., Sakai, A. & Collett, T., 1999. Elastic-wave velocity in marine sediments with gas hydrates: effective medium modeling, *Geophys. Res. Lett.,* **26,** 2021–2024.

Helgerud, M.B., Waite, W.F., Kirby, S.H. & Nur, A., 2009. Elastic wave speeds and moduli in polycrystalline ice Ih, sI methane hydrate, and sII methane-ethane hydrate, *J. geophys. Res.,* **114,** B02212.

Hesse, R., 2003. Pore anomalies of submarine gas hydrate zones as tool to assess hydrate abundance and distribution in the subsurface. What have we learned in the past decade?, *Earth Sci. Rev.,* **61,** 149–179.

Hester, K.C., Koh, C.A., Dec, S.F. & Sloan, E.D., 2008. Data report: gas hydrate structural and compositional characterization by spectroscopic analysis, IODP Expedition 311, In *Proc. IODP,* Vol. **311,** Riedel, M., Collett, T.S. & Malone, M.J., and the Expedition 311 Scientists, Integrated Ocean Drilling Program Management International, Inc., Washington, DC

Hill, R., 1963. Elastic properties of reinforced solids: some theoretical principles, *J. Mech. Phys. Solids,* **11,** 357–372.

Holland, M., Schultheiss, P., Roberts, J. & Druce, M., 2008. Observed gas hydrate morphologies in marine sediments, In: *6th Int. Conf. Gas Hydrates,* Vancouver, Canada.

Jain, A.K. & Juanes, R., 2009. Preferential Mode of gas invasion in sediments: grain-scale mechanistic model of coupled multiphase fluid flow and sediment mechanics, *J. geophys. Res.,* **114,** B08101.

Janik, A., Goldberg, D., Guerin, G. & Collett, T., 2009. Estimation of gashydrate saturation and heterogeneity on Cascadia margin from Ocean Drilling Project Leg 204 logging-while-drilling measurements, in *Natural gas hydrates—Energy resource potential and associated geologic hazards,* Vol. **89,** pp. 360–384. eds, Collett, T., Johnson, A., Knapp, C. & Boswell, R. American Association of Petroleum Geologists

Jenkins, J., Johnson, D., Ragione, L.L. & Makse, H., 2005. Fluctuations and the effective moduli of an isotropic, random aggregate of identical, frictionless spheres, *J. Mech. Phys. Solids,* **53,** 197–225.

Kim, H.S., Riedel, M., Ryu, B.J., Kim, G.Y. & Bahk, J.J., 2013. Improving gas hydrate saturation estimates using P-wave velocity log data by incorporating XRD-data for detailed matrix-mineralogy definition, *Mar. Pet. Geol.,* **47,** 155–167.

Kuhs, W.F., Genov, G., Goreshnik, E., Zeller, A., Techmer, K.S. & Bohrmann, G., 2004. The impact of porous microstructures of gas hydrates on their macroscopic properties, *International Journal of Offshore and Polar Engineering,* **14,** 305–309.

Kuhs, W.F., Kalpproth, A., Gotthardt, F., Techmer, K. & Heinrichs, T., 2000. The formation of meso- and macroporous gas hydrates, *Geophys. Res. Lett.,* **27,** 2929–2932.

Lee, M.W. & Collett, T.S., 2009. Gas hydrate saturations estimated from fractured reservoir at site NGHP-01-10, Krishna-Godavari basin, India, *J. geophys. Res.,* **114,** 261–281.

Liu, T., Bao, X.Y. & Guo, J.X., 2022. Modeling of seismic attenuation in fracture-filling gas hydrate-bearing sediments and its application to field observations in the Krishna-Godavari Offshore Basin India, *Mar. Petrol. Geol.,* **141,** 105 698.

Marín-Moreno, H., Sahoo, S.K. & Best, A.I., 2017. Theoretical modeling insights into elastic wave attenuation mechanisms in marine sediments with pore-filling methane hydrate, *J. Geophys. Res.: Solid Earth,* **122,** 1835–1847.

Mavko, G., Mukerji, T. & Dvorkin, J., 1998. *The Rock Physics Handbook,* Cambridge University Press.

Pabst, W. & Gregorová, E., 2013. Elastic properties of silica polymorphs–a review, *Ceramics,* **57,** 167–184.

Pan, H., Li, H., Zhang, J., Cai, S., Gui, Z. & Du, M., 2023. Joint elastic-electrical effective medium modeling for improved hydrate quantification, *Mar. Geophys. Res.,* **44**(2), 15.

Pan, H., Li, Y.G., Wei, C., Gui, Z.X., Li, X.M., Zhang, X., Zhao, Y. & Zhang, W., 2022b. Seismic rock-physics modeling of the complex-morphology hydrate reservoirs and applications, *Chin. J. Geophys.,* **65**(12), 4858–4873.

Pan, H.J. *et al.,* 2020. A unified contact cementation theory for gas hydrate morphology detection and saturation estimation from elastic-wave velocities, *Mar. Pet. Geol.,* **113,** 104146.

Pan, H.J., Li, H.B., Granab, D., Zhang, Y., Liu, T.Y. & Geng, C., 2019. Quantitative characterization of gas hydrate bearing sediment using elastic-electrical rock physics models, *Mar. Pet. Geol.,* **105,** 273–283.

Pan, H.J., Li, H.B., Wang, X.J., Cai, J.C., Qian, J., Howard, J.J. & Gao, Q., 2022a. A unified effective medium modeling framework for quantitative characterization of hydrate reservoirs, *Geophysics,* **87**(5), MR219–MR234.

Pride, S.R., 2003. Relationships between seismic and hydrological properties, In: *Hydrogeophysics ,* pp. 1–31, eds, Rubin, Y. & Hubbard, S., Kluwer Acad., New York

Reuss, A., 1929. Berechnung der Fliessgrenzen von Mischkristallen auf Grund der Plastizitaätsbedingung fuär Einkristalle, *Z. Ang. Math. Mech.,* **9,** 49–58.

Riedel, M., Collett, T.S. & Malone, M., 2010. Expedition 311 synthesis: scientific findings, In *Proc. IODP,* Vol. **311,** eds, Riedel, M., Collett, T.S. & Malone, M.J., and the Expedition 311 Scientists, Integrated Ocean Drilling Program Management International, Inc., Washington, DC

Riedel, M., Collett, T.S. & Malone, M.J.and the Expedition 311 Scientists, 2006. *Proc. IODP,* Vol. **311,** Integrated Ocean Drilling Program Management International, Inc., Washington, DC.

Rothwell, R.G., 1989. The Smear Slide Method, In: *Minerals and Mineraloids in Marine Sediments,* Springer, Dordrecht.

Ruppel, C.D., 2018. *Gas Hydrate in Nature,* 4pp., U.S. Geological Survey Fact Sheet 2017–3080,

Ruppel, C.D. & Kessler, J.D., 2017. The interaction of climate change and methane hydrates, *Rev. Geophys.,* **55,** 126–168.

Ruppel, C.D. & Waite, W.F., 2020. Grand challenge: timescales and processes of methane hydrate formation and breakdown, with application to geologic systems, *J. Geophys. Res.: Solid Earth,* **125,** e2018JB016459.

Sahoo, S.K. & Best, A.I., 2021. The influence of gas hydrate morphology on reservoir permeability and geophysical shear wave remote sensing, *J. Geophys. Res.: Solid Earth,* **126,** e2021JB022206.

Sahoo, S.K., Madhusudhan, B.N., MarínMoreno, H., North, L.J., Ahmed, S., Falcon-Suarez, I.H., Minshull, T.A. & Best, A.I., 2018a. Laboratory insights into the effect of sediment-hosted methane hydrate morphology on elastic wave velocity from time-lapse 4-D synchrotron X-ray computed tomography, *Geochem. Geophys. Geosyst.,* **19,** 4502–4521.

Sahoo, S.K., Marín-Moreno, H., North, L.J., Falcon-Suarez, I., Madhusudhan, B.N., Best, A.I. & Minshull, T.A., 2018b. Presence and consequences of coexisting methane gas with hydrate under two phase water-hydrate stability conditions, *J. Geophys. Res.: Solid Earth,* **123,** 3377–3390.

Sloan, E.D. & Koh, C.A., 2008. *Clathrate Hydrates of Natural Gases,* 3rd edn., 721pp., CRC Press, Taylor and Francis Group, New York

Spangenberg, E., 2001. Modeling of the influence of gas hydrate content on the electrical properties of porous sediments, *J. geophys. Res.,* **106**(B4), 6535–6548.

Stern, L.A. & Lorenson, T.D., 2014. Grain-scale imaging and compositional characterization of cryo-preserved India NGHP 01 gas-hydrate-bearing cores, *Mar. Pet. Geol.,* **58,** 206–222.

Stern, L.A., Lorenson, T.D. & Pinkston, J.C., 2011. Gas hydrate characterization and grainscale imaging of recovered cores from the Mount Elbert gas hydrate stratigraphic test well, Alaska North Slope, *Mar. Petrol. Geol.,* **28**(2), 394–403.

Suess, E., Torres, M.E., Bohrmann, G., Collier, R.W., Rickert, D., Goldfinger, C. *et al.*, 2001. Sea floor methane hydrates at hydrate ridge, Cascadia margin, In *Natural Gas Hydrates—Occurrence, Distribution and Detection,* pp. 87–98, American Geophysical Union, Washington, DC

Sultan, N. *et al.*, 2014. Pockmark formation and evolution in deep water Nigeria: rapid hydrate growth versus slow hydrate dissolution, *J. Geophys. Res.: Solid Earth,* **115,** 2679–2694.

Terry, D. & Knapp, C.C., 2018. A unified effective medium model for gas hydrates in sediments, *Geophysics,* **83**(6), MR317–MR332.

Terzariola, M., Parkb, J., Castrob, G.M. & Santamarina, J.C., 2020. Methane hydrate-bearing sediments: pore habit and implications, *Mar. Petrol. Geol.,* **116,** 104 302.

Torres, M.E., Teichert, B.M.A., Tréhu, A.M., Borowski, W. & Tomaru, H., 2004. Relationship of pore water freshening to accretionary processes in the Cascadia margin: fluid sources and gas hydrate abundance, *Geophys. Res. Lett.,* **31,** L22305.

Tréhu, A.M., Bohrmann, G., Rack, F. & Torres, M.E.and Leg 204 Scientific Party, 2003. *Proc. ODP, Initial Reports, 204 [CD-ROM]. Available from: Ocean Drilling Program,* pp. 77845–79547, Texas A&M University, College Station, TX

Tréhu, A.M., Long, P.E., Torres, M.E. *et al.*, 2004. Three-dimensional distribution of gas hydrate beneath southern Hydrate Ridge: constraints from ODP Leg 204, *Earth planet. Sci. Lett.,* **222**(3), 845–862.

Waite, W.F., Winters, W.J. & Mason, D.H., 2004. Methane hydrate formation in partially water-saturated Ottawa sand, *Am. Mineral.,* **89**(8–9), 1202–1207.

Wang, X.J., Hutchinson, D.R., Wu, S.G., Yang, S.X. & Guo, Y.Q., 2011. Elevated gas hydrate saturation within silt and silty clay sediments in the Shenhu area, South China Sea, *J. geophys. Res.,* **116,** B05102.

Yoneda, J., Kida, M., Konno, Y., Jin, Y., Morita, S. & Tenma, N., 2019. In situ mechanical properties of shallow gas hydrate deposits in the deep seabed, *Geophys. Res. Lett.,* **46,** 14459–14468.

Yu, Y.S., Zhang, X.W., Liu, J.W., Lee, Y. & Li, X.S., 2021. Natural gas hydrate resources and hydrate technologies: a review and analysis of the associated energy and global warming challenges, *Energy Environ. Sci.,* **14**(11), 5611–5668.

Yuan, T., Hyndman, R.D., Spence, G.D. & Desmons, B., 1996. Seismic velocity increase and deep-sea gas hydrate concentration above a bottom-simulating reflector on the northern Cascadia continental slope, *J. geophys. Res.,* **101,** 13 655–13 671.

Zhang, G. *et al.*, 2015. Geological features, controlling factors and potential prospects of the gas hydrate occurrence in the east part of the Pearl River Mouth Basin, South China Sea., *Mar. Pet. Geol.,* **67,** 356–367.

Zhu, X.Y., Liu, T., Ma, S., Liu, X.W. & Li, A.Y., 2023. Morphology identification of gas hydrate based on a machine learning method and its applications on saturation estimation, *Geophys. J. Int.,* **234**(2), 1307–1325.